Correspondence

Beampattern Synthesis for Frequency Diverse Array via Reweighted ℓ_1 Iterative Phase Compensation

This paper addresses the issue of beampattern synthesis with flexible magnitude response and low sidelobe in a frequency diverse array radar. It is formulated as an optimization problem in terms of ℓ_1-norm minimization, which encourages the sparsity of array pattern. An ℓ_1 iterative phase compensation (IPC) technique is employed to transform the nonconvex constraint to phase compensation form. Then, to further reduce the sidelobe level, a reweighted ℓ_1-IPC algorithm is devised, in which a sparsity-enhanced scheme is utilized to convert the ℓ_1-norm to a new cost function that more closely resembles ℓ_0-norm. Numerical results are presented to demonstrate the effectiveness of the proposed approach in different scenarios.

I. INTRODUCTION

Unlike traditional phased array radar [1], frequency diverse array (FDA) radar can suppress interferences in the range domain and thereby has received significant attention in the past few years [2]–[6]. The unique characteristic of FDA is that its beampattern is a function of angle and range. Moreover, when both angle and range distributions of FDA beampattern are controlled appropriately [3], [4], it is able to reject interferences with the same direction-of-arrival (DOA) as the target signal [5], [6].

In transmit beampattern design for FDA radar, a high sidelobe will lead to high false alarm probability, considerably degrading its performance in target detection. For sidelobe suppression of phased array radar, an efficient approach was suggested in [7] where the theory of Chebyshev polynomials is used to obtain a desired Dolph–Chebyshev pattern. The Chebyshev synthesis yields the narrowest beamwidth for a given uniform sidelobe level. In [8] and [9], least squares (LS) method is employed for computing a weight vector by minimizing sidelobe responses subject to a constrained mainlobe response, in which weight vector directly determines the formation of beampattern. The design can also be formulated as a linear program [10], and might efficiently be solved via convex optimization.

Manuscript received December 29, 2016; revised April 29, 2017; released for publication July 24, 2017. Date of publication August 3, 2017; date of current version February 7, 2018.

DOI. No. 10.1109/TAES.2017.2735638

Refereeing of this contribution was handled by S. D. Blunt.

This work was supported in part by the National Natural Science Foundation of China under Grant U1501253, Grant 61601304, Grant 61501300, Grant 61601300, and Grant 61501485, in part by the Natural Science Foundation of Guangdong Province under Grant 2015A030311030, in part by the Foundation of Shenzhen Government under Grant ZDSYS201507081625213, Grant KC2015ZDYF0023A, and Grant JCYJ20160520165659418, in part by the Foundation of China Postdoctoral Science under Grant 2015M582414 and Grant 2017M610547, and in part by the China Scholarship Council.

(Corresponding author: Lei Huang.)

However, when the estimated DOAs of the target and interferences are not accurate, the aforementioned methods may distort the target signal and the interferences may not be suppressed effectively. Therefore, an array pattern with flexible magnitude response over a wide angle region is preferred, where the magnitude response region should cover actual DOAs. In [11]–[14], several robust beamformers with magnitude response constraint are developed, which have the flexibility in controlling the beamwidth and response ripple in the desired region. However, the magnitude response constraint is nonconvex, which cannot be solved by the well-established convex programming techniques. To deal with this issue, semidefinite programming (SDP) [11], [13], autocorrelation sequence [12], and second-order cone programming (SOCP) [14] methods have been employed to transform the nonconvex optimization problem into a convex one. Nevertheless, the magnitude response methods do not take into account the range constraint and spatial sparsity of main beam.

Note that the pattern synthesis approaches mentioned above can be tailored for an FDA radar. Furthermore, we know that the beampattern of FDA usually has the sparse property because its mainbeam area is much smaller than the whole spatial range of interest. This motivates us to study the FDA pattern synthesis problem from the viewpoint of enhancing sparsity [15]. In this paper, enhancing sparsity refers to obtaining desired mainlobe response constraint and minimizing the response of overall sidelobe regions, which can be considered as making the response at sidelobe regions as close to zero as possible, i.e., as sparse as possible.

Specifically, the pattern synthesis for FDA radar transmitter is optimized by jointly considering flexible magnitude response and sidelobe suppression in this paper. In order to obtain an array pattern with flat-top covering desired target without distortion and flat-bottom rejecting interferences effectively, magnitude response constraints are designed to flexibly control its responses at those regions. Due to nonconvex constraints involved, the SDP, spectral factorization [16], and iterative SOCP approaches cannot be applied. To solve this problem, an ℓ_1 iterative phase compensation (IPC) technique is adopted to transform the nonconvex constraint into a convex phase compensation form. This allows us to produce the solution based on convex optimization. To further reduce the sidelobe level, a reweighted ℓ_1-IPC algorithm is also developed.

II. PROBLEM FORMULATION

A. FDA Array Model

Consider an FDA system with a uniform linear array (ULA) consisting of M transmit antennas. The carrier frequency at the mth element is expressed as

$$f_m = f_0 + (m-1)\cdot\Delta f, \quad m = 1, 2, \ldots, M \tag{1}$$

where f_0 denotes the reference carrier frequency, Δf is a small fixed-frequency increment, which is negligible compared with f_0. Note that Δf is a configurable parameter to control the beampattern of an FDA radar in range domain. Assume that the distance from the reference element to target is r and the corresponding DOA is θ. The steering vector of the FDA transmit array can be expressed as [4]

$$\boldsymbol{a}(\theta, r) = \left[1, e^{-j2\pi\left(\frac{d\sin\theta}{\lambda_0}+\frac{\Delta f r}{c}\right)} \cdots e^{-j2\pi(M-1)\left(\frac{d\sin\theta}{\lambda_0}+\frac{\Delta f r}{c}\right)}\right]^T \tag{2}$$

where d denotes the interelement spacing, λ_0 is the reference carrier wavelength, and c is the speed of light.

B. Sidelobe Suppression Model

The array pattern of FDA, denoted by $G(\theta, r)$, is

$$G(\theta, r) = \boldsymbol{w}^H \boldsymbol{a}(\theta, r), \quad \theta \in \boldsymbol{\Theta}, r \in \boldsymbol{R} \tag{3}$$

where $\boldsymbol{w}$ denotes the complex weight vector and $(\cdot)^H$ stands for the Hermitian transpose, $\boldsymbol{\Theta}$ is the whole angle region, and $\boldsymbol{R}$ denotes the range region detected by FDA radar. We could uniformly discretize $\boldsymbol{\Theta}$ and $\boldsymbol{R}$ into N and P points, respectively, to form the FDA steering matrix, which is expressed as $\boldsymbol{A} = [\boldsymbol{a}(\theta_1, r_1), \ldots, \boldsymbol{a}(\theta_1, r_P), \boldsymbol{a}(\theta_2, r_1), \ldots, \boldsymbol{a}(\theta_2, r_P), \ldots, \boldsymbol{a}(\theta_N, r_P)]$. Noticing that the steering vector of FDA $\boldsymbol{a}(\theta, r)$ is a function of θ and r, $\boldsymbol{A}$ is a matrix of dimensions $M \times NP$, which covers NP steering vectors in the whole angular and detected range regions.

Then, in order to minimize the sidelobe responses subject to mainlobe response satisfying magnitude response constraint, the beamformer design problem in angular and range domains is formulated based on the ℓ_0-norm minimization as

$$\begin{aligned} &\min_{\boldsymbol{w}} \left\|\boldsymbol{w}^H \boldsymbol{A}\right\|_0 \\ &\text{s.t. } L \le \left|\boldsymbol{w}^H \boldsymbol{a}(\theta, r)\right| \le U, \quad \theta \in \boldsymbol{\Theta}_s, r \in \boldsymbol{R}_s \end{aligned} \tag{4}$$

where $\|\cdot\|_0$ denotes the ℓ_0-norm, $|\cdot|$ is the modulus operator, L and U are the prescribed lower and upper bounds of the magnitude response, respectively, and $\boldsymbol{\Theta}_s$ as well as $\boldsymbol{R}_s$ denote the angle and range mainlobe regions.

However, the optimization problem in (4) is NP-hard and an ℓ_1-norm approximation is applied instead. To this end, the cost function in (4) becomes

$$\min_{\boldsymbol{w}} \left\|\boldsymbol{w}^H \boldsymbol{A}\right\|_1 \tag{5}$$

where $\|\cdot\|_1$ denotes the ℓ_1-norm. Subsequently, the optimization problem (4) is modified as

$$\begin{aligned} \min_{\boldsymbol{w}} \quad & \left\|\boldsymbol{w}^H \boldsymbol{A}\right\|_1 \\ \text{s.t. } & L \le \left|\boldsymbol{w}^H \boldsymbol{a}(\theta, r)\right| \le U, \quad \theta \in \boldsymbol{\Theta}_s, r \in \boldsymbol{R}_s \\ & \left|\boldsymbol{w}^H \boldsymbol{a}(\theta, r)\right| \le \varepsilon, \qquad \theta \in \boldsymbol{\Theta}_I, r \in \boldsymbol{R}_I \end{aligned} \tag{6}$$

where interference region constraint is added to form a pattern with flat-bottom rejecting interference significantly. In (6), $\boldsymbol{\Theta}_I$ and $\boldsymbol{R}_I$ are the angle and range null regions, respectively, and ε is user-defined upper bound for the magnitude response of null region. It should be noted that the constraint $L \le \left|\boldsymbol{w}^H \boldsymbol{a}(\theta, r)\right|$ is nonconvex, which implies that standard convex optimization tools cannot be directly utilized to solve this problem.

III. REWEIGHTED ℓ_1-IPC ALGORITHM

A. ℓ_1-IPC Algorithm Derivation

In this section, an ℓ_1-IPC approach is derived to solve the nonconvex optimization problem (6). First, let $\phi(\theta, r) \triangleq \angle\{\boldsymbol{w}^H \boldsymbol{a}(\theta, r)\}$ be the phase of $\boldsymbol{w}^H \boldsymbol{a}(\theta, r)$. Then, the constraint on the magnitude response $\left|\boldsymbol{w}^H \boldsymbol{a}(\theta, r)\right| \geq L$ is rewritten as

$$\left|\boldsymbol{w}^H \boldsymbol{a}(\theta, r)\right| = e^{-j\phi(\theta,r)} \boldsymbol{w}^H \boldsymbol{a}(\theta, r) \geq L. \tag{7}$$

Let $\bar{G}(\theta, r) = e^{-j\phi(\theta,r)} \boldsymbol{w}^H \boldsymbol{a}(\theta, r)$ be a new nominal array pattern, which should be a real number when $\phi(\theta, r)$ exactly matches $\angle\{\boldsymbol{w}^H \boldsymbol{a}(\theta, r)\}$. Therefore, the optimization problem (6) can be re-expressed as

$$\begin{aligned} \min_{\boldsymbol{w},\phi} \quad & \left\|\boldsymbol{w}^H \boldsymbol{A}\right\|_1 \\ \text{s.t.} \quad & \left|\boldsymbol{w}^H \boldsymbol{a}(\theta, r)\right| \leq U, && \theta \in \boldsymbol{\Theta}_s, r \in \boldsymbol{R}_s \\ & e^{-j\phi(\theta,r)} \boldsymbol{w}^H \boldsymbol{a}(\theta, r) \geq L, && \theta \in \boldsymbol{\Theta}_s, r \in \boldsymbol{R}_s \\ & \left|\boldsymbol{w}^H \boldsymbol{a}(\theta, r)\right| \leq \varepsilon, && \theta \in \boldsymbol{\Theta}_I, r \in \boldsymbol{R}_I. \end{aligned} \tag{8}$$

For the optimization problem (8), the objective function is a convex function and the constraints are convex sets over $\boldsymbol{w}$ and $\phi(\theta, r)$. However, CVX [17] and other standard convex optimization toolboxes cannot be applied because $\phi(\theta, r)$ appears in the exponential function in one of the constraints. For example, CVX utilizes symmetric primal/dual solvers, which do not directly support the exponential family functions [18]. Although successive approximation heuristic allows the symmetric primal/dual solvers to support the exponential family function, this method is an iterative approach, and converges slowly or even fails to converge [18].

It is clear that if the optimal value of $\phi(\theta, r)$ is known, (8) can be solved easily. However, the optimal $\phi(\theta, r)$ is determined by the optimal array weight $\boldsymbol{w}$. Thus, there is coupling between $\phi(\theta, r)$ and $\boldsymbol{w}$. In order to solve (8), we devise an alternating ℓ_1-IPC approach and apply CVX to find $\boldsymbol{w}$ at each iteration. First, the reasonable initial values of $\boldsymbol{w}_0$ and $\phi_0(\theta, r)$ should be determined. It should be noted that $\phi_0(\theta, r)$ might not align with the phase of $\boldsymbol{w}^H \boldsymbol{a}(\theta, r)$, that is to say, $\bar{G}(\theta, r)$ is generally a complex number, which is not admitted by CVX. To tackle this issue, the constraint $\bar{G}(\theta, r) \geq L$ in (8) is relaxed to $\mathrm{Re}\{\bar{G}(\theta, r)\} \geq L$, where $\mathrm{Re}\{\cdot\}$ stands for the real part operator. Then, the optimization problem (8) is approximated as

$$\begin{aligned} \min_{\boldsymbol{w},\phi} \quad & \left\|\boldsymbol{w}^H \boldsymbol{A}\right\|_1 \\ \text{s.t.} \quad & \left|\boldsymbol{w}^H \boldsymbol{a}(\theta, r)\right| \leq U, && \theta \in \boldsymbol{\Theta}_s, r \in \boldsymbol{R}_s \\ & \mathrm{Re}\{e^{-j\phi(\theta,r)} \boldsymbol{w}^H \boldsymbol{a}(\theta, r)\} \geq L, && \theta \in \boldsymbol{\Theta}_s, r \in \boldsymbol{R}_s \\ & \left|\boldsymbol{w}^H \boldsymbol{a}(\theta, r)\right| \leq \varepsilon, && \theta \in \boldsymbol{\Theta}_I, r \in \boldsymbol{R}_I. \end{aligned} \tag{9}$$

By solving (9), we finally obtain a suboptimal solution for (8). If a feasible $\boldsymbol{w}_0$ is provided, we have $\phi_0(\theta, r) = \angle\{\boldsymbol{w}_0^H \boldsymbol{a}(\theta, r)\}$. Subsequently, $\phi_0(\theta, r)$ is inserted into (9) to update the array weight $\boldsymbol{w}$. Similarly, the solution of $\boldsymbol{w}_k$ at the kth iteration is calculated by solving (9) at $\phi_{k-1}(\theta, r)$ which is obtained by $\phi_{k-1}(\theta, r) = \angle\{\boldsymbol{w}_{k-1}^H \boldsymbol{a}(\theta, r)\}$. The iterative process is plotted in Fig. 1 to illustrate the convergence of the ℓ_1-IPC approach. As iteration number increases, $\mathrm{Re}\{\bar{G}_k(\theta, r)\}$ becomes larger whereas the imaginary component reduces. Subsequently, $\bar{G}(\theta, r)$ turns out to be a real number. As a result, the algorithm can be terminated when a specified maximum number of iterations K are reached. The ℓ_1-IPC approach is tabulated in Algorithm 1.

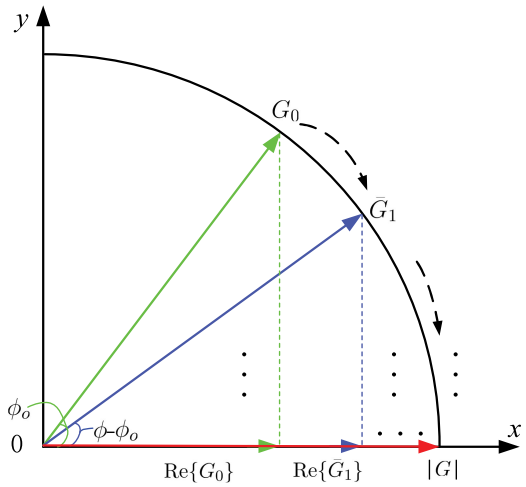

Fig. 1. Convergence illustration of $\bar{G}(\theta, r)$.

Algorithm 1: ℓ_1-IPC Algorithm.

Input: $K, \boldsymbol{A}, U, L, \varepsilon, \boldsymbol{\Theta}_s, \boldsymbol{R}_s, \boldsymbol{\Theta}_I, \boldsymbol{R}_I$

Step 1. Initialize $\boldsymbol{w}$: Solve (13) to determine $\boldsymbol{w}_0$

for $k = 0, 1, \ldots, K$ **do**

Step 2. Update $\phi_k(\theta, r)$:

$$\phi_k(\theta, r) = \angle\{\boldsymbol{w}_k^H \boldsymbol{a}(\theta, r)\}, \ \theta \in \boldsymbol{\Theta}_s, r \in \boldsymbol{R}_s \tag{10}$$

Step 3. Update $\boldsymbol{w}_{k+1}$:

$$\begin{aligned} \min_{\boldsymbol{w}_{k+1}} \quad & \left\|\boldsymbol{w}_{k+1}^H \boldsymbol{A}\right\|_1 \\ \text{s.t.} \quad & \left|\boldsymbol{w}_{k+1}^H \boldsymbol{a}(\theta, r)\right| \leq U, && \theta \in \boldsymbol{\Theta}_s, r \in \boldsymbol{R}_s \\ & \mathrm{Re}\{e^{-j\phi_k(\theta,r)} \boldsymbol{w}_{k+1}^H \boldsymbol{a}(\theta, r)\} \geq L, && \theta \in \boldsymbol{\Theta}_s, r \in \boldsymbol{R}_s \\ & \left|\boldsymbol{w}_{k+1}^H \boldsymbol{a}(\theta, r)\right| \leq \varepsilon, && \theta \in \boldsymbol{\Theta}_I, r \in \boldsymbol{R}_I \end{aligned} \tag{11}$$

end for

Output: $\boldsymbol{w}_{K+1}$.

The initialization procedure for $\boldsymbol{w}$ in Step 1 is explained as follows. First, assuming that the phase $\phi(\theta, r)$ is known, we have

$$\begin{aligned} \mathrm{Re}\{e^{-j\phi(\theta,r)} \boldsymbol{w}^H \boldsymbol{a}(\theta, r)\} &= e^{-j\phi(\theta,r)} \boldsymbol{w}^H \boldsymbol{a}(\theta, r) \\ &= \left|\boldsymbol{w}^H \boldsymbol{a}(\theta, r)\right| \\ &\geq \mathrm{Re}\{\boldsymbol{w}^H \boldsymbol{a}(\theta, r)\}. \end{aligned} \tag{12}$$

Therefore, the constraint $\mathrm{Re}\{e^{-j\phi(\theta,r)} \boldsymbol{w}^H \boldsymbol{a}(\theta, r)\} \geq L$ in (9) could be further relaxed as $\mathrm{Re}\{\boldsymbol{w}^H \boldsymbol{a}(\theta, r)\} \geq L$. When $\mathrm{Re}\{\boldsymbol{w}^H \boldsymbol{a}(\theta, r)\} \geq L$, $\mathrm{Re}\{e^{-j\phi(\theta,r)} \boldsymbol{w}^H \boldsymbol{a}(\theta, r)\} \geq L$ is satis-

fied. The optimization problem (9) is then approximated as

$$\begin{aligned}\min_{\boldsymbol{w}} \ & \left\|\boldsymbol{w}^H\boldsymbol{A}\right\|_1 \\ \text{s.t.} \ & \left|\boldsymbol{w}^H\boldsymbol{a}(\theta,r)\right| \le U, \qquad \theta\in\boldsymbol{\Theta}_s, r\in\boldsymbol{R}_s \\ & \mathrm{Re}\{\boldsymbol{w}^H\boldsymbol{a}(\theta,r)\} \ge L, \quad \theta\in\boldsymbol{\Theta}_s, r\in\boldsymbol{R}_s \\ & \left|\boldsymbol{w}^H\boldsymbol{a}(\theta,r)\right| \le \varepsilon, \qquad \theta\in\boldsymbol{\Theta}_I, r\in\boldsymbol{R}_I \end{aligned} \tag{13}$$

which does not involve the phase parameter $\phi(\theta,r)$ and can be solved easily by a standard convex optimization tool. It should be noted that (13) is only employed for initializing $\boldsymbol{w}_0$ in Step 1 of the ℓ_1-IPC algorithm. Of course, other initialization schemes of $\boldsymbol{w}_0$ can also be used. According to our results in Section IV, $\boldsymbol{w}_0$ yielded by (13) is able to boost the convergence rate, that is, we attain a minimum of the objective function only within a few iterations.

In order to further illustrate the convergence of the ℓ_1-IPC method, we set

$$\boldsymbol{w}^H\boldsymbol{a}(\theta,r) = Be^{j\phi(\theta,r)}, \theta\in\boldsymbol{\Theta}_s, r\in\boldsymbol{R}_s \tag{14}$$

where B is the magnitude of $\boldsymbol{w}^H\boldsymbol{a}$. From (14), we easily obtain $e^{-j\phi(\theta,r)}\boldsymbol{w}^H\boldsymbol{a}(\theta,r) = B$ in (8) and $\mathrm{Re}\{e^{-j\phi_k(\theta,r)}\boldsymbol{w}_{k+1}^H\boldsymbol{a}(\theta,r)\} = B\cos(\phi_{k+1}-\phi_k)$ in (11). The purpose of our algorithm is to make $\phi_{k+1}-\phi_k$ tend to 0. As shown in Fig. 1, when the number of iterations increases, $\mathrm{Re}\{\bar{G}\}$ becomes closer to $\left|\boldsymbol{w}^H\boldsymbol{a}(\theta,r)\right|$. Once $\mathrm{Re}\{\bar{G}\}$ is equal to $\left|\boldsymbol{w}^H\boldsymbol{a}(\theta,r)\right|$, the final solution is obtained.

B. Reweighted ℓ_1-IPC Algorithm

Recall that the cost function in (9), i.e., ℓ_1-norm of the sparse vector $\boldsymbol{w}^H\boldsymbol{A}$, is equivalent to its ℓ_0-norm only when all nonzero values in the sparse vector are equal to one, which, however, cannot be guaranteed in the optimization process. This in turn indicates that there is a performance gap resulting from the replacement of ℓ_0-norm with ℓ_1-norm in the objective function. This motivates us to devise a new penalty function that more closely resembles the ℓ_0-norm.

Considering that the mainbeam gains at the desired angle and range regions are kept around one and the pattern gains at other regions are expected to be zero, we employ the reweighted ℓ_1-norm minimization scheme [15] to reform the objective function in the ℓ_1-IPC scheme, which is denoted as reweighted ℓ_1-IPC algorithm. The purpose is to further reduce the sidelobe of array pattern. In the reweighted ℓ_1-IPC algorithm, we introduce a parameter vector $\boldsymbol{q}$ that is associated with $\boldsymbol{w}$ in the iterative process. Here, $\boldsymbol{q}$ is a vector of length Q, which equals the number of columns in $\boldsymbol{A}$, that is, its length is chosen such that the dimension of array pattern $\boldsymbol{w}^H\boldsymbol{A}$ can be matched.

The reweighted ℓ_1-IPC algorithm is tabulated in Algorithm 2, where $\circ$ in (15) stands for the Hadamard product and μ in (16) should satisfy $\mu > 0$. The μ is introduced to provide stability and make sure $(\boldsymbol{q}_i)_{k+1}$ is meaningful when some elements in $\boldsymbol{w}_{k+1}^H\boldsymbol{A}$ are close to zero. According to [15], μ is set smaller than the expected nonzero magnitudes of $\boldsymbol{w}^H\boldsymbol{A}$.

Algorithm 2: Reweighted ℓ_1-IPC Algorithm

Input: K, $\boldsymbol{A}$, U, L, ε, μ, $\boldsymbol{\Theta}_s$, $\boldsymbol{R}_s$, $\boldsymbol{\Theta}_I$, $\boldsymbol{R}_I$, Q

Step 1. Initialize $\boldsymbol{q}$ and $\boldsymbol{w}$:

$(\boldsymbol{q}_i)_0 = 1, \quad i = 1,2,\ldots,Q$

Solve (13) to determine $\boldsymbol{w}_0$

for $k = 0,1,\ldots,K$ **do**

Step 2. Update $\phi_k(\theta,r)$ via (10)

Step 3. Update $\boldsymbol{w}_{k+1}$ using:

$$\begin{aligned}\min_{\boldsymbol{w}_{k+1}} \ & \left\|\boldsymbol{q}_k\circ\left(\boldsymbol{w}_{k+1}^H\boldsymbol{A}\right)\right\|_1 \\ \text{s.t.} \ & \left|\boldsymbol{w}_{k+1}^H\boldsymbol{a}(\theta,r)\right| \le U, \qquad \theta\in\boldsymbol{\Theta}_s, r\in\boldsymbol{R}_s \\ & \mathrm{Re}\{e^{-j\phi_k(\theta,r)}\boldsymbol{w}_{k+1}^H\boldsymbol{a}(\theta,r)\} \ge L, \ \theta\in\boldsymbol{\Theta}_s, r\in\boldsymbol{R}_s \\ & \left|\boldsymbol{w}_{k+1}^H\boldsymbol{a}(\theta,r)\right| \le \varepsilon, \qquad \theta\in\boldsymbol{\Theta}_I, r\in\boldsymbol{R}_I \end{aligned} \tag{15}$$

Step 4. Update $(\boldsymbol{q}_i)_{k+1}$ using:

$$(\boldsymbol{q}_i)_{k+1} = \frac{1}{\left|\boldsymbol{w}_{k+1}^H\boldsymbol{A}\right|+\mu}, \quad i = 1,2,\ldots,Q \tag{16}$$

end for

Output: $\boldsymbol{w}_{K+1}$.

In this iterative process, there is coupling among $\boldsymbol{q}$, $\phi(\theta,r)$, and $\boldsymbol{w}$. The $\boldsymbol{q}$ could further adjust the cost function in (15) and make it more closely resemble the ℓ_0-norm compared with the cost function in (11).

IV. SIMULATION RESULTS

In this simulation, we consider an FDA radar equipping with a ULA with $M = 13$ omnidirectional sensors. The carrier frequencies are equally spaced with $\Delta f = 1$ kHz starting from reference frequency $f_0 = 8$ GHz. The interelement spacing d is set to half minimum wavelength, i.e., $d = \frac{1}{2}\lambda_M = \frac{1}{2}\frac{c}{f_0+M\Delta f}$. Assign $\boldsymbol{\Theta} = [-90^\circ, 90^\circ]$ and $\boldsymbol{R} = [0, 400]$ km, where $\boldsymbol{\Theta}$ and $\boldsymbol{R}$ are uniformly discretized with step sizes 0.5° and 1 km, respectively, i.e., $N = 361$ and $P = 401$. Also, we set $L = 10^{-r_{\mathrm{db}}/20}$, $U = 10^{r}_{\mathrm{db}}/20$, and $\varepsilon = 10^{a_{\mathrm{db}}/20}$, where r_{db} and a_{db} denote the beam ripple and null attenuation in decibel, respectively. We assign $r_{\mathrm{db}} = 0.2$ dB, $a_{\mathrm{db}} = -80$ dB and the maximum number of iterations $K = 6$. To compare the performances of the proposed algorithms with those of the state-of-the-art approaches, the LS [8], SDP-spectral factorization [11], and SDP-principal component [19] algorithms are considered. For the LS method, mainlobe response is formulated as $\|\boldsymbol{w}^H\boldsymbol{a}(\theta,r)-1\|_2 \le \sigma, \theta\in\boldsymbol{\Theta}_s, r\in\boldsymbol{R}_s$, and $\sigma = 0.2$ dB. In the SDP-spectral factorization and SDP-principal component algorithms, we assign an array weight matrix $\boldsymbol{W} = \boldsymbol{w}\boldsymbol{w}^H$. Moreover, according to the ℓ_1-IPC algorithm, we consider the Dolph–Chebyshev [7] method to enhance the constraint. The parameter μ in the reweighted ℓ_1-IPC method is set to 0.1 unless stated otherwise. The CVX [17] is employed to solve the optimization problems. For sake of simplicity, the SDP-spectral factorization, SDP-principal

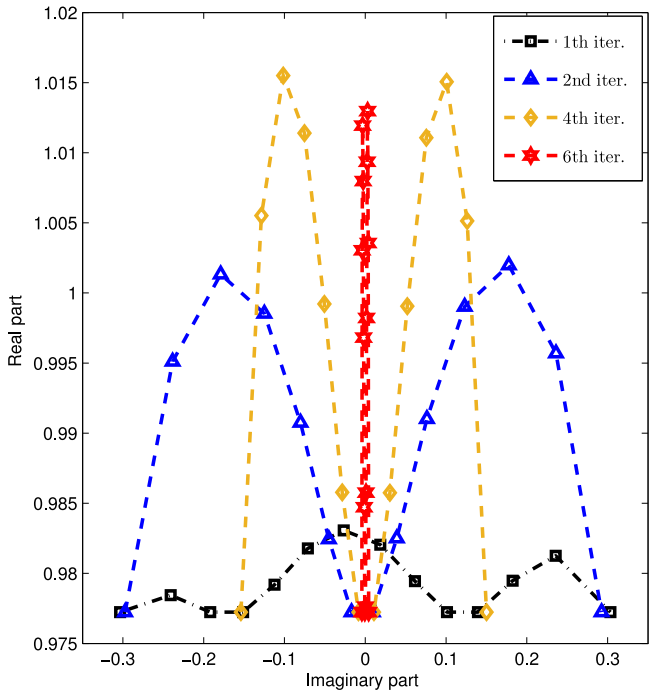

Fig. 2. Imaginary and real parts of $\bar{\boldsymbol{g}}$ versus iteration number.

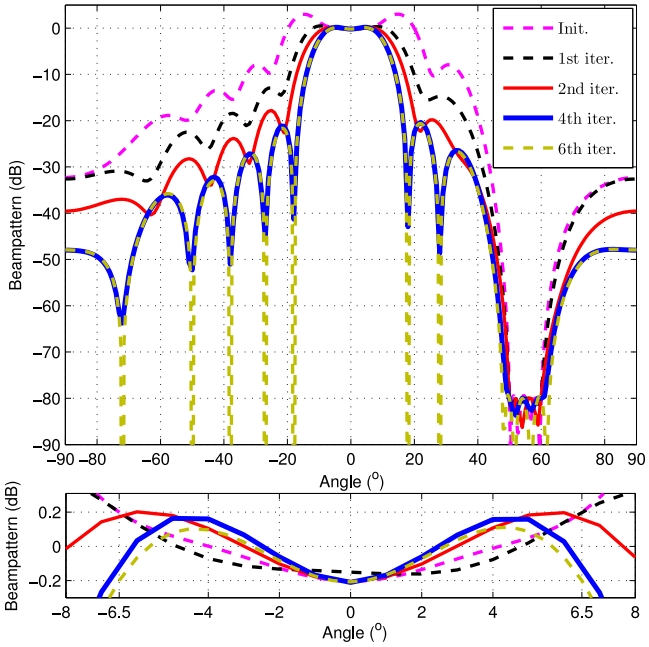

Fig. 3. Beampattern of ℓ_1-IPC in angle domain.

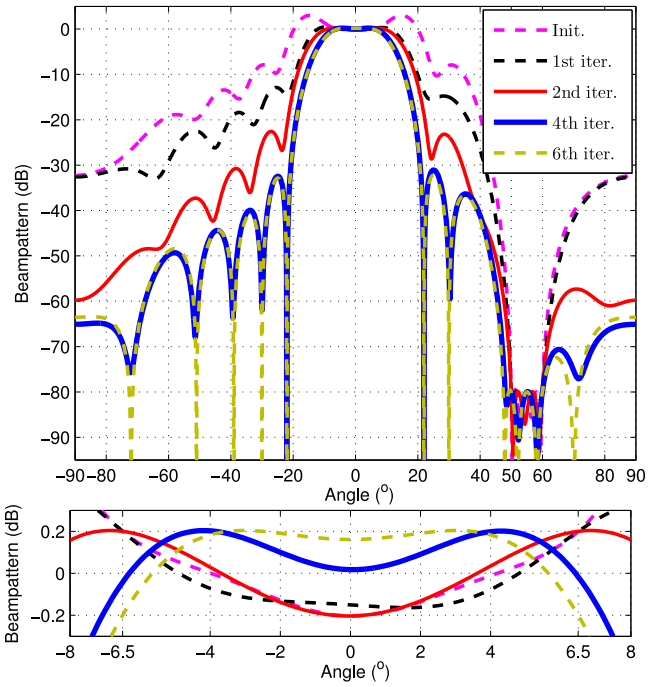

Fig. 4. Beampattern reweighted ℓ_1-IPC in angle domain.

component, and Dolph–Chebyshev IPC algorithms are abbreviated as SDP-SF, SDP-PC, and DC-IPC algorithms, respectively.

EXAMPLE 1 In the first test, the range from the reference element to both the desired target and interference is $r = 200$ km. The DOAs of the desired target and interference are located in the regions $\boldsymbol{\Theta}_s = [-6.5^\circ, 6.5^\circ]$ and $\boldsymbol{\Theta}_I = [50^\circ, 60^\circ]$, respectively, where $\boldsymbol{\Theta}_s$ and $\boldsymbol{\Theta}_I$ are both uniformly discretized with step sizes 1°. In this case, the Chebyshev window with 20 dB of sidelobe attenuation is used. For notational simplicity, the beampattern formed by the initial weight $\boldsymbol{w}_0$ in (13) is denoted as "Init.".

Fig. 2 plots the convergence of $\bar{G}(\theta, r), \theta \in \boldsymbol{\Theta}_s$ versus the iteration number. Here, $\bar{G}(\theta, r), \theta \in \boldsymbol{\Theta}_s$ is abbreviated as $\bar{\boldsymbol{g}}$, which includes 14 array pattern values because $\boldsymbol{\Theta}_s$ has been uniformly discretized into 14 points. As the number of iterations increases, the imaginary parts of $\bar{\boldsymbol{g}}$ approach zero whereas its real parts converge to 1. It is observed that at the sixth iteration, the imaginary parts of $\bar{\boldsymbol{g}}$ are almost equal to 0.

The beampatterns of the ℓ_1-IPC and reweighted ℓ_1-IPC algorithms are shown in Figs. 3 and 4, respectively. It is seen that both approaches can successfully form the mainbeams in the region of $\boldsymbol{\Theta}_s = [-6.5^\circ, 6.5^\circ]$ and nulls in the region of $\boldsymbol{\Theta}_I = [50^\circ, 60^\circ]$. Also, the null attenuation satisfies the given constraints. Moreover, we observe that the sidelobe level decreases gradually with the iteration number. In order to intuitively display the upper and lower limits of the main lobe, the lower subfigures in Figs. 3 and 4 show the details of main lobes. We see that the values of main lobe response are within $[-0.2, 0.2]$ dB at $\boldsymbol{\Theta}_s = [-6.5^\circ, 6.5^\circ]$, which satisfies the lower and upper bound constraints.

It is seen from Fig. 3 that the mainlobe and null of all tested methods except the SDP-PC method cover the signal and interference regions, respectively. The SDP-PC scheme has good performance in sidelobe and null, but its mainlobe cannot completely cover the signal regions. This is because the weight matrix $\boldsymbol{W}$ obtained is not of rank-one. Using the spectral factorization technique, the SDP-SF method can solve the problem when the rank $\boldsymbol{W}$ is not one. In addi-

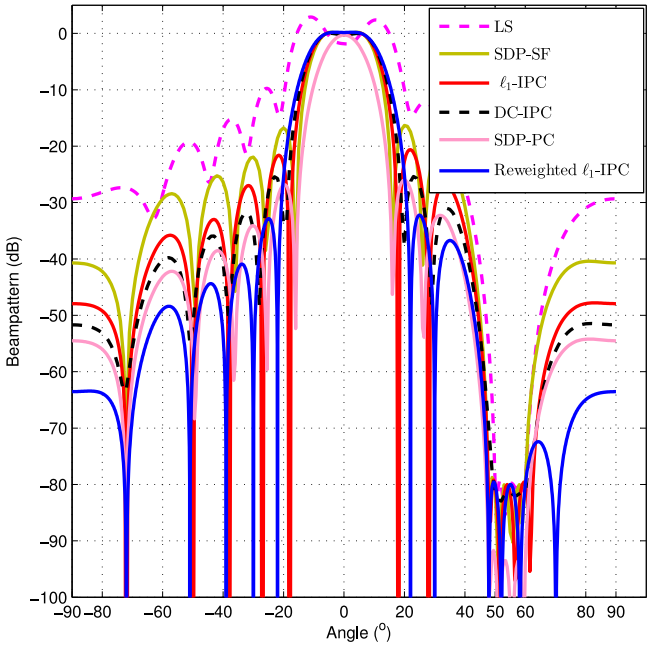

Fig. 5. Beampattern comparison in angle domain.

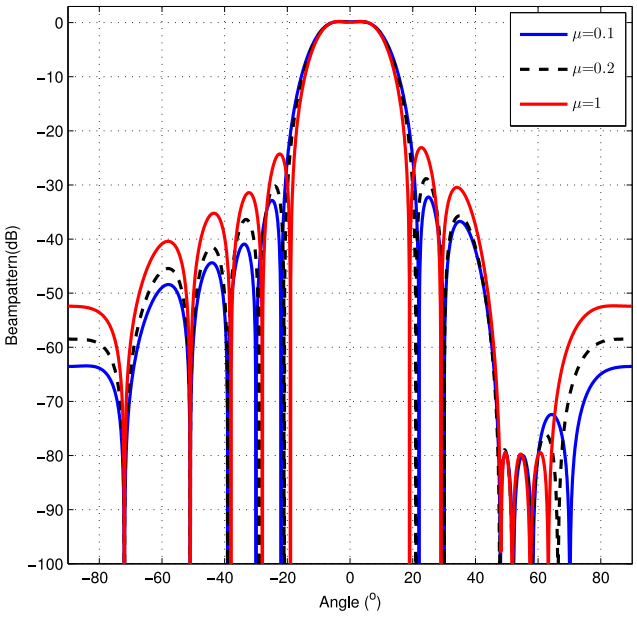

Fig. 6. Beampattern of reweighted ℓ_1-IPC, in angle domain, $\mu = [0.1, 0.2, 1]$.

tion, the sidelobes of the ℓ_1-IPC, Dolph–Chebyshev IPC and reweighted ℓ_1-IPC algorithms are generally lower than those of the LS and SDP-SF methods after six iterations. It is observed that some sidelobes of the LS algorithm are higher than its mainlobe, which causes a high false-alarm probability. Furthermore, the mainbeam of LS algorithm is obviously wider than those of other methods. The mainlobe of the reweighted ℓ_1-IPC method is a little bit wider than those of other tested algorithms. But the sidelobes of the reweighted ℓ_1-IPC algorithm are the lowest in all the investigated methods, because the reweighted objective function more closely resembles the ℓ_0-norm compared with ℓ_1-norm. Therefore, the reweighted ℓ_1-IPC algorithm is able to save more energy for target probing than other approaches.

In order to study the effect of μ on the beampattern in the reweighted ℓ_1-IPC approach, Fig. 6 depicts, at the sixth iteration, the beampattern comparison for different μ, that is, $\mu = [0.1, 0.2, 1]$. We observe that as μ decreases, the sidelobe level of beampattern decreases gradually and the mainlobe becomes wider slightly. Furthermore, to examine the convergence behaviors of the ℓ_1-IPC and reweighted ℓ_1-IPC algorithms, Fig. 7 depicts the ℓ_1-norm of beampattern gain, i.e., $\|\boldsymbol{w}^H\boldsymbol{A}\|_1$, at each iteration. It is seen that the values of $\|\boldsymbol{w}^H\boldsymbol{A}\|_1$ for both the ℓ_1-IPC and reweighted ℓ_1-IPC algorithms decrease rapidly and converge at the sixth iteration. At the first iteration, because each element in the vector $\boldsymbol{q}$ is initialized as 1, the optimization problem (15) is equivalent to (11). This is why the ℓ_1-IPC and reweighted ℓ_1-IPC algorithms produce the same solution $\boldsymbol{w}$, which contributes to the same value of $\|\boldsymbol{w}^H\boldsymbol{A}\|_1$ in Fig. 7. After the first iteration, the values of $\|\boldsymbol{w}^H\boldsymbol{A}\|_1$ of the reweighted ℓ_1-IPC algorithm with $\mu = [0.1, 0.2, 1]$ are all smaller than those of the ℓ_1-IPC algorithm. Moreover, for the reweighted ℓ_1-IPC

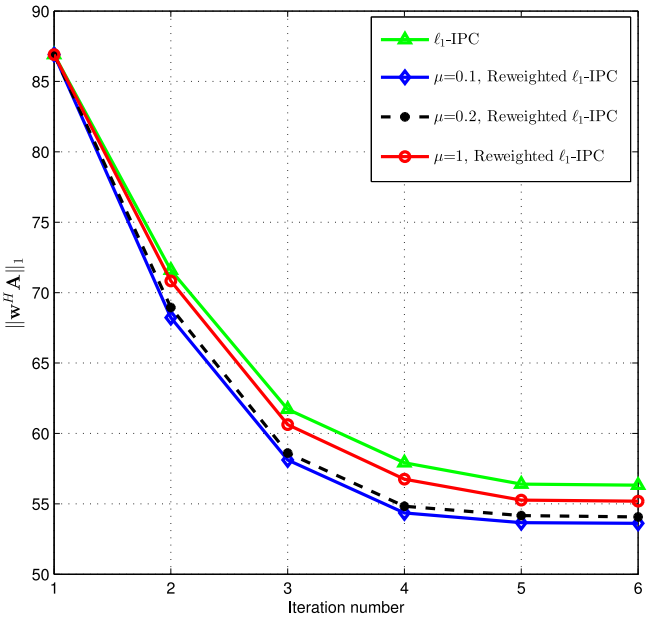

Fig. 7. $\|\boldsymbol{w}^H\boldsymbol{A}\|_1$ versus iteration number in angle domain.

algorithm, the values of $\|\boldsymbol{w}^H\boldsymbol{A}\|_1$ for $\mu = 0.1$ are much lower than those of $\mu = [0.2, 1]$, which is consistent with the beampattern in Fig. 6. As a result, the reweighted ℓ_1-IPC algorithm with $\mu = 0.1$ has the lowest sidelobe and the smallest values of $\|\boldsymbol{w}^H\boldsymbol{A}\|_1$ compared with other cases.

EXAMPLE 2 In this scenario, the DOAs of desired target and interference are both assumed to be 0°. Under such an environment, it is impossible for the conventional phased array radar to reject the interference. The ranges from the reference element to the desired target and interference are located in the regions of $\boldsymbol{R}_s = [190, 210]$ km and $\boldsymbol{R}_I = [95, 105]$ km, respectively. In this case,

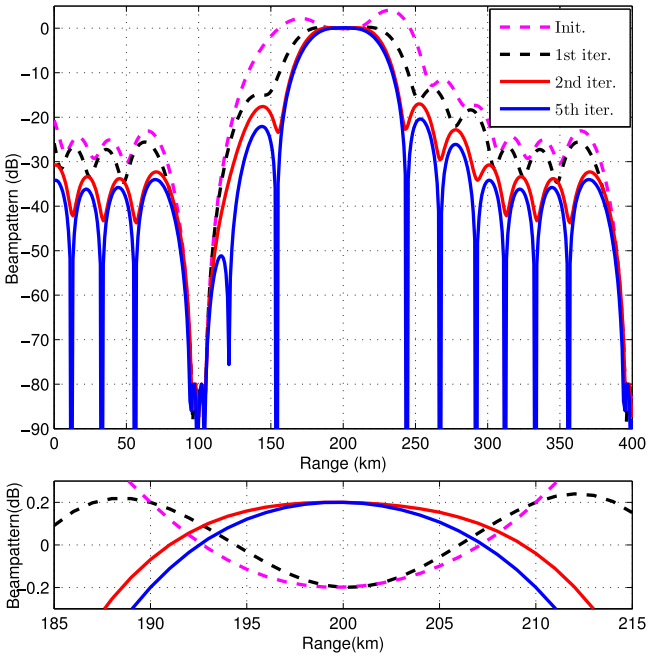

Fig. 8. Beampattern of ℓ_1-IPC in range domain.

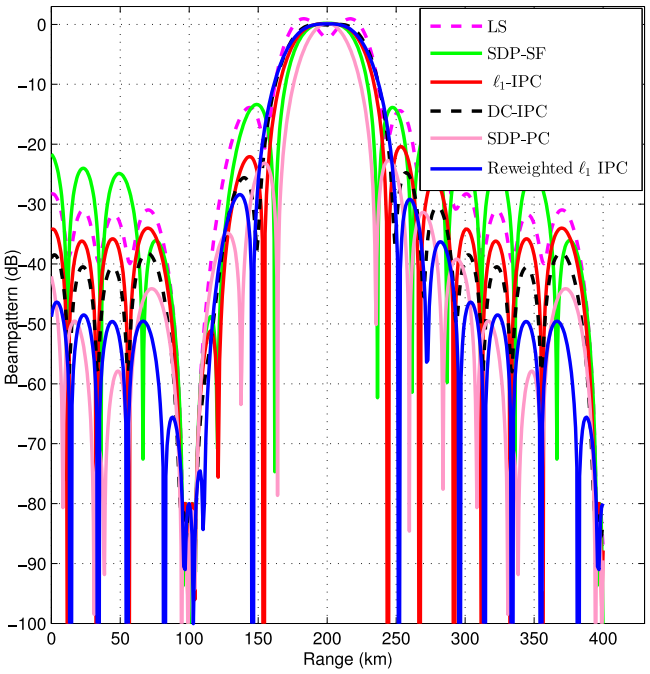

Fig. 10. Beampattern comparison in range domain.

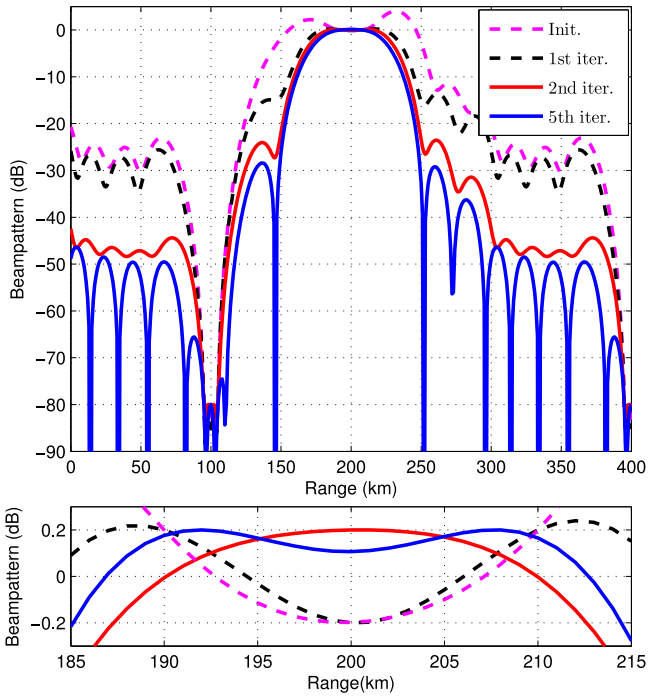

Fig. 9. Beampattern of reweighted ℓ_1-IPC in range domain.

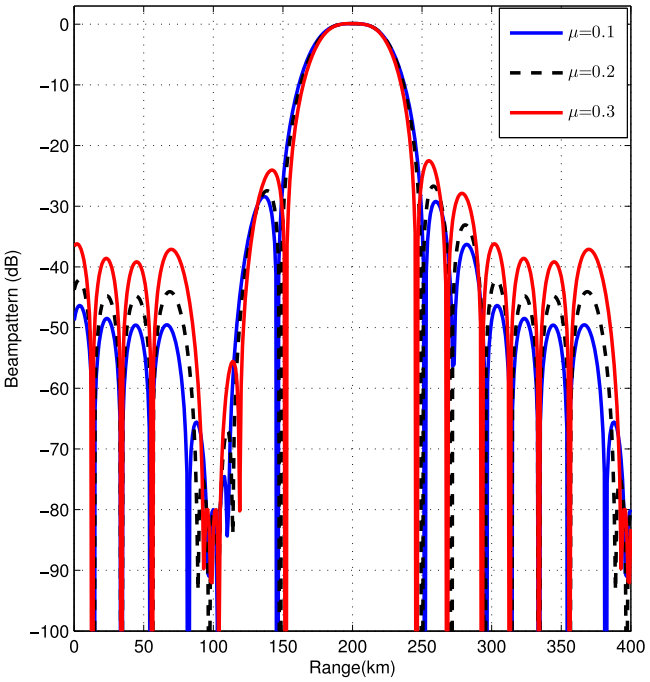

Fig. 11. Beampattern of reweighted ℓ_1-IPC in range domain, μ=[0.1, 0.2, 1].

the Chebyshev window with 25 dB of sidelobe attenuation is employed. Similarly, the beampattern formed by the initial weight $\boldsymbol{w}_0$ in optimization problem (13) is denoted as "Init.".

Figs. 8 and 9 plot the beampatterns of the ℓ_1-IPC and reweighted ℓ_1-IPC algorithms, respectively. Herein, the numerical results of the initial case, first, second, and fifth iterations are provided. It is observed that the methods tested can successfully provide the mainbeams in the region of $\boldsymbol{R}_s = [190, 210]$ km and nulls in the region of $\boldsymbol{R}_I = [95, 105]$ km. Also, the enlargement of mainbeams can be confirmed in the lower subfigures of Figs. 8 and 9, which satisfy the designated constraints of lower and upper bounds. Moreover, when the iteration number increases, the sidelobe level decreases gradually.

The patterns of the LS, SDP-SF, ℓ_1-IPC, SDP-PC, DC-IPC, and reweighted ℓ_1-IPC algorithms are shown

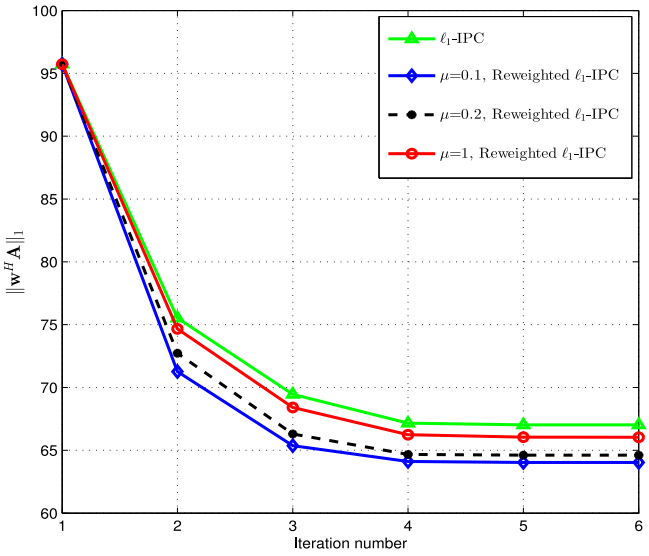

Fig. 12. $\|\boldsymbol{w}^H\boldsymbol{A}\|_1$ versus iteration number in range domain.

in Fig. 10. The result is similar to that of Fig. 5, except that some sidelobes of the SDP-SF algorithm are higher than those of the LS algorithm and some sidelobes of the SDP-PC algorithm are lower than those of the reweighted ℓ_1-IPC algorithm. It is obvious that the reweighted ℓ_1-IPC algorithm generally offers satisfactory performance in mainlobe and sidelobe simultaneously. Hence, the power transmitted by the FDA radar can be focused on the target. To examine the influence of μ on the reweighted ℓ_1-IPC approach, we present the beampatterns of the reweighted ℓ_1-IPC scheme for different μ in Fig. 11 and the value of $\|\boldsymbol{w}^H\boldsymbol{A}\|_1$ at each iteration in Fig. 12. It is seen in Fig. 11 that the sidelobe level of beampattern decreases gradually and the mainlobe becomes a little bit wider as μ decreases. It is indicated in Fig. 12 that, with the increase of the iteration number, the values of $\|\boldsymbol{w}^H\boldsymbol{A}\|_1$ for both the ℓ_1-IPC and reweighted ℓ_1-IPC algorithms quickly decrease and converge to constant values. Note that the convergence curves in Fig. 12 are similar to those in Fig. 7, which implies that the reweighted ℓ_1-IPC method is superior to the ℓ_1-IPC algorithm in terms of low-sidelobe beampattern synthesis.

V. CONCLUSION

The pattern synthesis with flexible magnitude response and low sidelobe is devised for the transmitter of FDA radar in this paper. To employ the spatial sparsity of the beampattern as well as the direction and range constraints, an ℓ_1-IPC approach is devised, which transforms and solves the ℓ_1-norm minimization problem with nonconvex constraint. In order to further reduce the sidelobe level of beampattern, the reweighted ℓ_1-IPC method is developed by iteratively refining the ℓ_1-norm cost function, ending up with a new objective function that is closer to the ℓ_0-norm. Numerical results have confirmed the superiority of the proposed approach over several existing schemes. In our future work, we will consider other reweighting rules and low-sidelobe constraint on the weights of the waveforms to further enhance the performance of FDA radar.

QIANG LI
LEI HUANG, *Senior Member, IEEE*
Shenzhen University, Shenzhen 518060, China
E-mail: (liqiang198780@163.com; lhuang8sasp@hotmail.com)

HING CHEUNG SO, *Fellow, IEEE*
City University of Hong Kong, Hong Kong, China
E-mail: (hcso@ee.cityu.edu.hk)

HUIFENG XUE
Twelfth Research Institute, China Aerospace Science and Technology Group, Beijing 100048, China
E-mail: (xhf0616@163.com)

PEICHANG ZHANG
Shenzhen University, Shenzhen 518060, China
E-mail: (pzhang@szu.edu.cn)

REFERENCES

[1] A. Charlish, K. Woodbridge, and H. Griffiths
Phased array radar resource management using continuous double auction
IEEE Trans. Aerosp. Electron. Syst., vol. 51, no. 3, pp. 2212–2224, Jul. 2015.

[2] P. Antonik, M. C. Wicks, H. D. Griffiths, and C. J. Baker
Frequency diverse array radars
In *Proc. IEEE Radar Conf.*, New York, USA, Apr. 2006, pp. 215–217.

[3] P. F. Sammartino, C. J. Baker, and H. D. Griffiths
Frequency diverse MIMO techniques for radar
IEEE Trans. Aerosp. Electron. Syst., vol. 49, no. 1, pp. 201–222, Jan. 2013.

[4] W. Q. Wang
Subarray-based frequency diverse array radar for target range-angle estimation
IEEE Trans. Aerosp. Electron. Syst., vol. 50, no. 4, pp. 3057–3067, Oct. 2014.

[5] J. W. Xu, S. Q. Zhu, and G. S. Liao
Range ambiguous clutter suppression for airborne FDA-STAP radar
IEEE J. Sel. Top. Signal Process., vol. 9, no. 8, pp. 1620–1631, Dec. 2015.

[6] J. W. Xu, G. S. Liao, S. Q. Zhu, L. Huang, and H. C. So
Joint range and angle estimation using MIMO radar with frequency diverse array
IEEE Trans. Signal Process., vol. 63, no. 13, pp. 3396–3410, Apr. 2015.

[7] C. L. A. Dolph
Current distribution for broadside arrays which optimizes the relationship between beam width and side-lobe level
Proc. IRE, vol. 34, no. 6, pp. 335–348, Jun. 1946.

[8] W. Liu and S. Weiss
Wideband Beamforming: Concepts and Techniques. New York, NY, USA: Wiley, 2010.

[9] P. You, Y. Liu, X. Huang, L. Zhang, and Q. H. Liu
Efficient phase-only linear array synthesis including coupling effect by GA-FFT based on least-square active element pattern expansion method
Electron. Lett., vol. 51, pp. 791–792, May 2015.

[10] S. Kwak, J. Chun, D. Park, Y. K. Ko, and B. L. Cho
Asymmetric sum and difference beam pattern synthesis with a common weight vector
IEEE Antennas Wireless Propag. Lett., vol. 15, pp. 1622–1625, 2016.

[11] Z. L. Yu, M. H. Er, and W. A. Ser
Novel adaptive beamformer based on semidefinite programming (SDP) with magnitude response constraints
IEEE Trans. Antennas Propag., vol. 56, no. 5, pp. 1297–1307, May 2008.

[12] Z. L. Yu, W. Ser, M. H. Er, Z. Gu, and Y. Li
Robust adaptive beamformers based on worst-case optimization and constraints on magnitude response
IEEE Trans. Signal Process., vol. 57, no. 7, pp. 2615–2628, Jul. 2009.

[13] Z. L. Yu, Z. Gu, J. Zhou, Y. Li, W. Ser, and M. H. Er
A robust adaptive beamformer based on worst-case semidefinite programming
IEEE Trans. Signal Process., vol. 58, no. 11, pp. 5914–5919, Nov. 2010.

[14] S. A. Vorobyov, A. B. Gershman, and Z. Q. Luo
Robust adaptive beamforming using worst-case performance optimization: A solution to the signal mismatch problem
IEEE Trans. Signal Process., vol. 51, no. 2, pp. 313–324, Feb. 2003.

[15] E. J. Candès, M. B. Wakin, and S. P. Boyd
Enhancing sparsity by reweighted ℓ_1 minimization
J. Fourier Anal. Appl., vol. 14, no. 5, pp. 877–905, Oct. 2008.

[16] S. E. Nai, W. Ser, Z. L. Yu, and S. Rahardja
A robust adaptive beamforming framework with beampattern shaping constraints
IEEE Trans. Antennas Propag., vol. 57, no. 7, pp. 2198–2203, Jul. 2009.

[17] M. Grant and S. Boyd
CVX: Matlab software for disciplined convex programming version 2.1, build 1110, Jun. 2015. [Online]. Available: http://cvxr.com/cvx

[18] M. Grant and S. Boyd
CVX users guide
version 2.1, pp. 69–70, Mar. 2017. [Online]. Available: http://web.cvxr.com/cvx/ doc/CVX.pdf

[19] Z. Q. Luo, W.-K. Ma, A. M. C. So, Y. Ye, and S. Zhang
Semidefinite relaxation of quadratic optimization problems
IEEE Signal Process. Mag., vol. 27, no. 3, pp. 20–34, May 2010.